Int. J. Electrochem. Sci., 16 **(2021)** Article Number: 211023, doi: 10.20964/2021.10.18

International Journal of
ELECTROCHEMICAL
SCIENCE
www.electrochemsci.org

Anode Material for Lithium-Ion Batteries Based on MoS_2 and Conductive Polymer Binder: Effects of Electrode Thickness

A. I. Volkov, E. G. Tolstopjatova, V. V. Kondratiev[*]

Institute of Chemistry, Saint Petersburg State University, Universitetskaya nab. 7/9, Saint Petersburg, 199034
[*]E-mail: vkondratiev@mail.ru

Received: 5 June 2021 / *Accepted:* 20 July 2021 / *Published:* 10 September 2021

High specific capacity of anode materials based on MoS_2 is attractive for their use in lithium-ion batteries. However, low cycling stability of bulk MoS_2 and complicated conversion mechanism of charge storage are major challenges for adoption of such materials as anodes for lithium-ion batteries. In this work, we focus on the effects of electrode thickness on electrochemical performance of anodes based on MoS_2. We assess whether variation of thickness is a viable strategy to enhance the stability of such materials. Among electrodes with thickness varied within 70-250 μm, those with 100 μm to 150 μm material thickness display the most favorable rate capability in galvanostatic charge-discharge tests (32% of initial capacity at 2 A g^{-1}), which is linked to their low charge transfer resistance, as shown by electrochemical impedance spectroscopy. We also show that conductive polymer binder based on PEDOT:PSS and CMC facilitates charge transfer, as compared to conventional PVDF binder. Electrochemical studies and investigations with SEM, HR-XRD, and XPS methods show that irreversible processes occur in the electrodes and point at the necessity of substantial MoS_2 materials modification to preserve their stability.

Keywords: anode material; conducting polymer; PEDOT:PSS; molybdenum disulfide; electrode thickness; lithium-ion batteries

1. INTRODUCTION

Molybdenum disulfide has gained significant attention as a battery anode material [1–3]. It is a two-dimensional nanomaterial with a layered graphene-like structure with expected interlayer Li^+ intercalation. 2H and 1T are the most reported polytypes of MoS_2. 2H-MoS_2 occurs naturally and is a preferred one for use in electrode materials. In 2H-MoS_2 each Mo atom is coordinated with six S atoms, and each S atom is coordinated with three Mo atoms, providing hexagonal unit cell [4]. Trigonal polytype 1T-MoS_2 is usually a product of the processes in the electrode materials involving interaction

of initial 2H-MoS_2 with intercalated ions. Hexagonally structured layers of MoS_2 are stacked into multilayers by weak van der Waals forces between S-Mo-S layers [5]. The interlayer distance is tunable via various synthesis and exfoliation methods [6–8]. Expanded interlayer spacing, coupled with possibility of surface modification, makes the material suitable for hosting a wide selection of metal ions, including Li [9,10], Na [11,12], K [13], Mg [14], and Zn [15]. Large efforts are employed to replace graphite with MoS_2 in lithium-ion batteries anodes. Its intermediate lithiation voltage (ca. 1.1 – 2.0 V vs. Li/Li^+) is compensated by high specific capacity that well exceeds the theoretical value and may reach up to (800 – 1300) mA h g^{-1} [16–20], especially when used with carbon materials. High specific capacity is a result of complex processes occurring with the material after initial discharge. The capacity derived from lithiation (1) of MoS_2 should be 167 mA h g^{-1}, and the following conversion of Li_xMoS_2 to metallic molybdenum (2) adds up to 669 mA h g^{-1}.

$$MoS_2 + x\cdot Li^+ + x\cdot e^- \rightarrow Li_xMoS_2 \qquad \text{Eq. 1}$$

$$Li_xMoS_2 + (4 - x)\cdot Li^+ + (4 - x)\cdot e^- \rightarrow Mo + 2Li_2S \qquad \text{Eq. 2}$$

The evidence for these reactions has been provided in several studies involving in situ and operando XRD [21], XAS [21], and TEM [22] techniques, as well as computational research [23,24]. Yet, the reported capacity values are often much higher than that. There are several contributions to enhanced energy storage properties [1,3,19]. These include adsorption of lithium species on molybdenum, emergence of new electrochemical processes involving Li_2S and S, and effects linked to increased surface area.

Reaction (2) is likely irreversible, as bulk molybdenum is rarely able to form sulfides at standard temperature. Mo nanoparticles, however, may serve as adsorption sites for lithium ions [20].

Further, lithium sulfide formed in reaction (2) opens a possibility of the process (3), which is commonly reported as the main one in lithium-sulfur batteries [25], where MoS_2 can be used in cathode materials [26,27]. Theoretical capacity of this reaction is 1167 mA h g^{-1} [28]. This value is hardly likely to be reached, as we must take the mass of molybdenum-containing species into account. Yet the overwhelming evidence points that process (3) becomes the main one in batteries with MoS_2-based anode from the second cycle onwards, as MoS_2 sheets are gradually consumed [20,29,30].

$$S + 2Li^+ + 2e^- \rightarrow Li_2S \qquad \text{Eq. 3}$$

Two main approaches to enhance the electrochemical properties of MoS_2 are usually employed. The majority of considered MoS_2 materials are hybrid structures with carbon materials, various additives, conductive and stabilizing agents [1,19,31]. A second option is MoS_2 composites with graphene and other 2D layered structures for construction of MoS_2 aligned layers due to the structural similarities [31–34]. Additionally, micro- and nanostructured materials are generally reported to have higher capacities and stabilities than their bulk counterparts [35], including MoS_2 [36]. Better surface availability may be one of the reasons.

Indeed, thermogravimetric analysis shows that the specific surface area of initial material can reach more than 150 m^2 g^{-1} [26]. However, it is difficult to determine the surface area of the material during cycling, especially considering irreversibility of the reaction (2) and formation of new electrochemical species that inevitably distort the structure. Despite that, increased capacity and stability are strong enough evidence that the resulting structures are beneficial for electrochemical properties. This may be another indication that molybdenum nanoparticles coordinate lithium upon reduction

(capacity contribution) and capture polysulfides (stability enhancement). The latter, i.e., polysulfide shuttling, is a major problem in lithium-sulfur batteries [37,38], and reaction (3) points at the necessity of mitigating the same problem in MoS_2-based anodes.

The issue of thickness effects on electrode performance is an important one and has been studied for Li-ion intercalation cathode materials [39]. To the best of our knowledge, there is no published literature on the dependence of MoS_2-based anode materials performance on electrode thickness. Moreover, the discussion of the main reasons affecting the stability and high utilization of energy storage remains inconclusive for MoS_2. The importance of chemical bonding between the components of electrodes or adsorption and chemical interactions with surfaces, as well as relative contribution of these factors to increased performance and stability, is yet to be estimated.

In this work, we report on anodes for lithium-ion batteries based on molybdenum disulfide and conductive PEDOT:PSS/CMC binder with various thicknesses of the active material layer. Conductive PEDOT:PSS/CMC binder in MoS_2 anodes was shown previously to be beneficial for cell properties and is thus used here as a primary object [40]. We substantiate our claims of better charge transfer kinetics of materials with conductive PEDOT:PSS/CMC binder by cyclic voltammetry and electrochemical impedance spectroscopy.

We present novel results of a systematic investigation of the effect of the thickness of MoS_2-based electrodes on the functional properties of assembled half-cells. The variation of thickness allowed to find the trade-off between hindered charge transfer in thicker electrodes and increased polysulfides dissolution in thinner electrodes. A variety of electrochemical methods and material characterization techniques allows us to hypothesize the reasons of material behavior.

In addition, regardless of the initial characteristics of the MoS_2 material obtained by different synthesis methods, the study of thickness effect is important, since most of the reported information on the high performance is given in the literature either for impractical testing conditions with very small mass loadings, that are not acceptable for real batteries, or for composites (e.g., MoS_2/graphene) that disregard the properties of standalone MoS_2.

The results are similar to earlier research data on intercalation type of electrode materials [41]. The presented study is intended to provide more information on the performance of conversion-type MoS_2-based electrodes and for their further development.

2. EXPERIMENTAL

2.1. Electrodes and cells preparation

Conductive binder PEDOT:PSS/CMC was prepared by adding carboxymethyl cellulose (MTI Corp.) to PEDOT:PSS (poly(3,4-ethylenedioxythiophene):polystyrene sulfonate) 1.3% aqueous dispersion (Aldrich) in 1:1 ratio and thorough mixing. Electrode composition was prepared by mixing MoS_2 powder (90 nm diameter particles) (Aldrich) with carbon black "Super P" (Timcal Inc.) and conductive binder as per Table 1. 4 ml of deionized water (≥18 MΩ resistivity, obtained using Millipore Direct-Q UV) per 100 mg of dry components was used to prepare the slurry. The slurry was coated on

copper foil (9 μm thickness) using a blading technique with a gap of 20 μm, 70 μm, 100 μm, 150 μm, and 250 μm. The coatings were denoted $MoS_{cond\text{-}CB\text{-}h}$, where *h* is corresponding blade gap. The coatings were dried under vacuum at 60 °C overnight. The coatings were then calendered with a gap of 50 μm. The disks (*d* = 14 mm) that were then used as electrodes were cut out and weighted. The average mass loading was 0.07 mg cm^{-2} for $MoS_{cond\text{-}CB\text{-}20}$, 0.39 mg cm^{-2} for $MoS_{cond\text{-}CB\text{-}70}$, 0.52 mg cm^{-2} for $MoS_{cond\text{-}CB\text{-}100}$, 0.73 mg cm^{-2} for $MoS_{cond\text{-}CB\text{-}150}$, and 1.6 mg cm^{-2} for $MoS_{cond\text{-}CB\text{-}250}$. The MoS_2-based electrodes were assembled in CR2032 half-cells with double Celgard 2400 separators (*d* = 16 mm) and Li foil (*d* = 12 mm, 0.6 mm thickness, Aldrich) as anode. 6 drops of 1 mol dm^{-3} $LiPF_6$ in 1:1 (v/v) EC/DEC (Aldrich) were added as electrolyte.

Table 1. Ratios of components for preparation of electrode compositions.

Composition	Active material, wt. %	Carbon black, wt. %	Binder, wt. %
$MoS_{cond\text{-}CB\text{-}h}$	70	20	10 (PEDOT:PSS/CMC)
MoS_{cond}	90	0	10 (PEDOT:PSS/CMC)
MoS_{PVDF}	70	20	10 (PVDF)

For reference to earlier work [40], electrodes without carbon black, denoted MoS_{cond}, were prepared with 90 wt. % MoS_2 and 10 wt. % PEDOT:PSS (150 μm thickness, 1.3 mg cm^{-2}). For comparison with standard procedures of electrode manufacturing, the cells with PVDF (Aldrich) binder were prepared in a 70:20:10 MoS_2/carbon black/PVDF ratio (150 μm thickness, 1.4 mg cm^{-2}) using NMP (Aldrich) as a solvent for slurry preparation. The drying temperature was 120 °C in this case. The rest of the procedures was the same as above. The samples with PVDF binder were denoted as MoS_{PVDF}.

2.2. Materials characterization

Morphology of the samples was studied using scanning electron microscopy (SEM) (SUPRA 40VP Carl Zeiss, Germany). High-resolution X-ray diffraction (HR-XRD) (Bruker-AXS D8 DISCOVER, Cu-Kα, λ = 0.15406 nm) and X-ray photoelectron spectroscopy (XPS) (Thermo Fisher Scientific Escalab 250Xi) were employed to study the chemical composition of the samples.

2.3. Electrochemical characterization

All electrochemical studies were done at room temperature (~22±2 °C).

Galvanostatic charge-discharge measurements (GCD) were performed on an automatic GCD battery cell test instrument (Neware Co., China) in the potential range between 3.0 V and 0.05 V (vs. Li/Li^+). Current densities from 100 mA g^{-1} to 2000 mA g^{-1} (per MoS_2 mass) were used for C-rate measurements. Cycle life of the cells was evaluated at 100 mA g^{-1}. The procedures always started with a discharge from the open-circuit voltage. The reported capacities are normalized to MoS_2 mass.

Cyclic voltammetry (CV) and electrochemical impedance spectroscopy (EIS) were performed on an Autolab PGSTAT 30 potentiostat/galvanostat (Eco-Chemie, Netherlands). For CV measurements, the potential range was (0.05 — 3.00) V, scan rate was 0.1 mV s^{-1}, unless stated otherwise. Electrochemical impedance spectra were obtained at open-circuit voltage and specific charging (discharging) states of the cell. Before recording impedance spectra, the cells were conditioned for 1 h at a given cell voltage to achieve a steady state. The amplitude was 5 mV rms, the values were obtained in 100 kHz to 0.01 Hz frequencies range. The spectra were fitted to equivalent circuit models using Nova 2.1.5 software.

3. RESULTS AND DISCUSSION

3.1. Selection of optimal binder

As we have recently reported [40], PEDOT:PSS/CMC conductive binder can effectively replace PVDF in MoS_2-based anodes, improving their initial specific capacity. The thickness of electrodes was 50 µm, which provided less than desired for commercial batteries mass loadings of ~0.7 mg cm^{-2}. In the development of this approach, we aimed to increase mass loadings to make commercially viable anodes. Thus, for reference to $MoS_{cond\text{-}CB\text{-}150}$ samples, we have prepared anodes with higher mass loading: MoS_{cond} coatings (1.3 mg cm^{-2}) and MoS_{PVDF} coatings (1.4 mg cm^{-2}) with 150 µm thickness.

Cyclic voltammetry allows monitoring the difference in electrochemical processes depending on the composition. The cycles from 1st to 3rd are presented for the sample $MoS_{cond\text{-}CB\text{-}150}$ in (Figure 1a) as they show the typical behavior of all samples on the initial cycle. The two main cathodic peaks in the first scan are at 0.83 V and 0.38 V. First, Li_xMoS_2 forms through lithium intercalation into the MoS_2 structure at 0.83 V (1). This is accompanied by 2H to 1T phase transformation [42], as Li^+ position in the octahedral cavity in van de Waals gap is especially favorable in the case of 1T-Li_xMoS_2 host lattice [43]. Then, an intense cathodic peak at 0.38 V indicates conversion of MoS_2 to Li_2S and metallic molybdenum (2). The intensity of the peak also suggests that the solid electrolyte interphase (SEI) layer forms here [44]. Similarly, sharp peaks of Li_xMoS_2 formation and conversion to Li_2S and Mo overlapping with SEI formation are present for the MoS_{PVDF} sample (Figure 1b), at 0.93 V and 0.40 V, respectively. The same processes occur for the MoS_{cond} sample (Figure 1c), albeit the peak at 0.39 V is distinctly prolonged to the more negative area, suggesting inhibited charge transfer capability.

Cathodic peaks of the first cycle are significantly less pronounced in the following cycles, as new cathodic processes arise due to the emergence of new phases. For $MoS_{cond\text{-}CB\text{-}150}$ (Figure 1a) the cathodic peaks at 2.13 V, 1.94 V, 1.12 V, and 0.31 V may be assigned to the processes earlier explored in the literature. The peaks at 2.13 V and 1.94 V are related to long-chain polysulfides (Li_2S_6, Li_2S_4) formation from S_8, as known from studies of Li-S systems, followed by conversion to short-chain sulfides Li_2S and Li_2S_2 [45]. The peak at 1.12 V relates to intercalation of Li^+ into remaining MoS_2 [22,46]. Peaks of the same nature are located at 2.09 V, 1.90 V, and 1.10 V for the MoS_{PVDF} (Figure 1b) sample. The 0.31 V peak of $MoS_{cond\text{-}CV\text{-}150}$ material is assigned to further Li_xMoS_2 conversion to Mo nanoparticles embedded into Li_2S environment [47]. The intensity of the 0.31 V peak is greatly diminished, which fits well in the

concept of degradation of MoS_2 and Li_2S/S becoming the main redox pair. The peaks related to the same process shift even more negative for the MoS_{PVDF} sample: 0.27 V in the second cycle, and 0.15 V in the third one. This drift might be explained by the lack of conductivity in this sample, as compared to MoS_{cond} (Figure 1c), though the intensities of the peaks are similar.

The first anodic sweep for the $MoS_{cond\text{-}CB\text{-}150}$ sample contains only one dominant peak at 2.31 V. Consistently with the literature, it indicates Li_2S electrochemical conversion to long-chain polysulfides and sulfur [48], yet the process of Li^+ deintercalation may also occur here [22]. This peak remains in the following cycles. A weak peak at ~1.70 V arises on the second and following cycles. It may be attributed to oxidation of higher-order polysulfide species [49], or oxidation of molybdenum to Mo(VI) [22]. These peaks are also present in cyclic voltammetry curves for the MoS_{PVDF} sample, with a notable difference in the shape. Here, the main conversion peak shifts from 2.32 V to 2.43 V over three consecutive cycles and significantly widens. This, again, points at the lack of conductivity of MoS_{PVDF}, which is additionally impaired by combination of non-conductive binder and components: Li_2S, polysulfides, and sulfur. The oxidation peak is more consistent within initial cycles for $MoS_{cond\text{-}CB\text{-}150}$, than for MoS_{PVDF}, which may be related to increased availability of the active material via enhanced conductivity provided by PEDOT:PSS/CMC binder. Upon application of MoS_{cond} with 150 μm thickness, we observe a decrease in overall electrochemical characteristics as compared to previously reported 50 μm thickness [40]. As seen clearly from the comparison of CVs in Figure 1, the intensity of the 2.1 V / 1.9 V redox pair related to the Li_2S/S system drops drastically. This is due to lack of conductivity in absence of carbon black, and PEDOT:PSS alone does not facilitate satisfactory fast charge transfer in the bulk of the material. The present low-conductive Li_2S thus cannot fully convert to sulfur, which leads to extremely low current densities and nearly flat shapes of voltammograms.

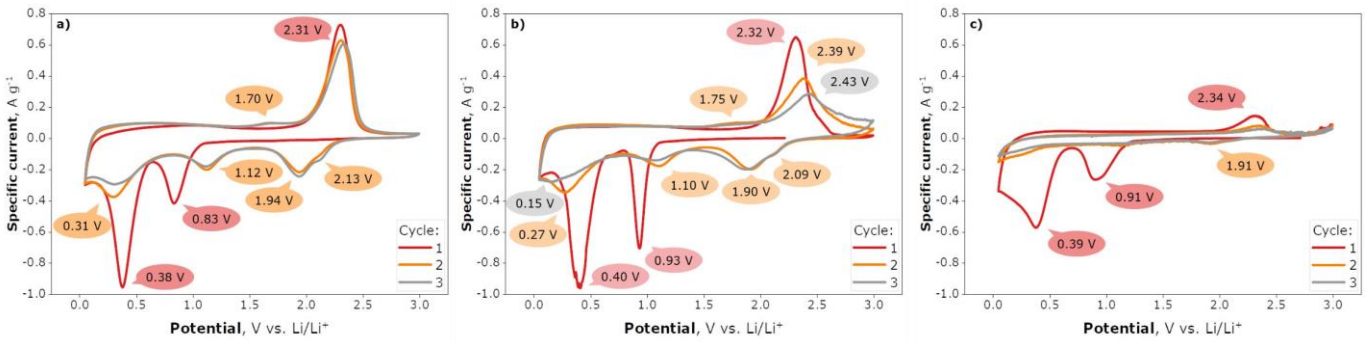

Figure 1. 1st to 3rd cyclic voltammetry cycles of a) $MoS_{cond\text{-}CB\text{-}150}$, b) MoS_{PVDF}, and c) MoS_{cond} samples at 0.1 mV s^{-1}.

Galvanostatic charge-discharge (GCD) curves of the second cycle for $MoS_{cond\text{-}CB\text{-}150}$, MoS_{cond}, and MoS_{PVDF} compositions are presented in Figure 2a. Similar to CVs of these electrodes, both compositions with carbon black demonstrate significantly higher capacities than the composition with only conductive PEDOT:PSS binder. The plateaus of the reduction and oxidation processes are also more pronounced for $MoS_{cond\text{-}CB\text{-}150}$ and MoS_{PVDF}. At least three poorly resolved plateaus are present in

discharge curves, which match the processes described for CV peaks. Upon charging, the main process occurs in ca. (2.2—2.5) V range, which is oxidation of Li_2S with formation of sulfur and polysulfides.

The charge curves of samples with carbon black also feature an area with an almost constant slope from 0.05 V to ca. 2.2 V, with a slight inflection at ~1.6 V. This line corresponds to near-constant current on CVs and may be ascribed to capacitive (e.g., the capacity of adsorbed Li^+ ions) processes in the material [50], meaning that we cannot associate full capacity value with purely faradaic processes.

As expected, cycle life of MoS_{cond} (Figure 2b) turns out to be the lowest for the studied samples. This means the replacement of standard binder and carbon black with only conductive binder brings no advantage at higher mass loadings. However, bringing carbon black back into the electrode composition is beneficial. This is seen from the initial capacity values of the $MoS_{cond\text{-}CB\text{-}150}$ sample. The capacity of the 1st charge cycle is 1040 mA h g^{-1}, 970 mA h g^{-1}, and 410 mA h g^{-1} for $MoS_{cond\text{-}CB\text{-}150}$, MoS_{PVDF}, and MoS_{cond}, respectively. Another thing that is obvious from the presented plot is the general trend of capacity decrease for all samples. After 100 cycles, the capacity value of all samples lays in the (105—125) mA h g^{-1} range. This indicates that regardless of the chosen composition, the active material suffers irreversible transformations making it electrochemically inactive. The loss of capacity may be ascribed to full irreversible conversion of MoS_2 to Li_2S and Mo, accompanied by volumetric expansion, which damages SEI film, and causes it to deplete electrolyte by continuous growth [1,29]. The lowest initial capacity of carbon black-free MoS_{cond} sample is likely due to disconnected active particles and insufficient electronic contact. It makes the majority of MoS_2 agglomerates unavailable for recharging, and the performance gets even worse as most of the remaining MoS_2 transforms into sulfur. On the contrary, the use of both conducting polymer and conductive carbon black provides more electronic pathways than PVDF with carbon black [51]. SO_3^- groups in PEDOT:PSS can also provide electrostatic shielding within the material preventing polysulfide dissolution (in addition to covalent binding by MoS_2), which has been explored in Li-S membranes [52] and cathodes [53]. Both $MoS_{cond\text{-}CB\text{-}150}$ and MoS_{PVDF} demonstrate >95% initial coulombic efficiency, which stabilizes closer to 100% as the recharging continues.

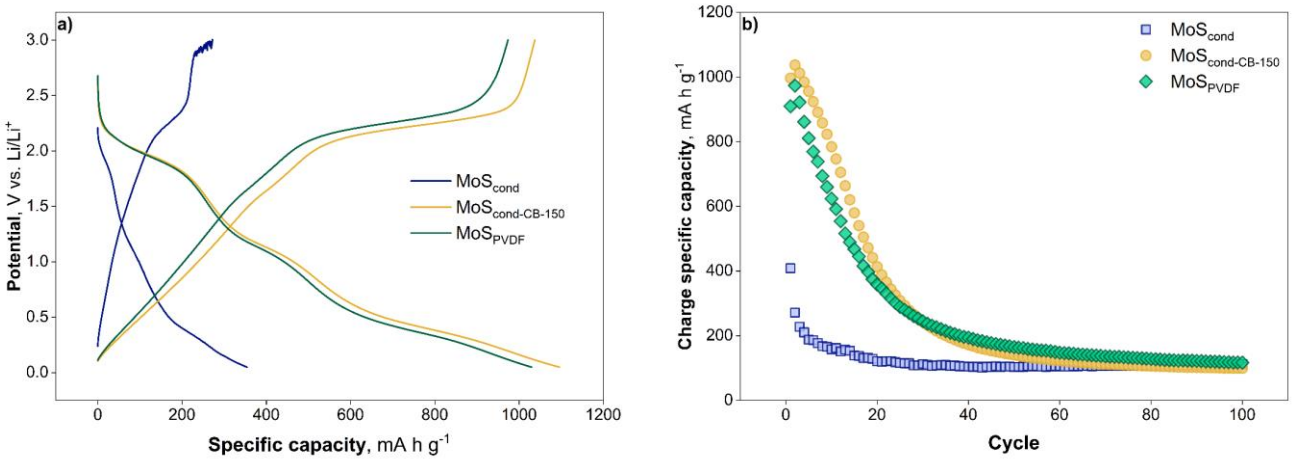

Figure 2. a) Galvanostatic charge-discharge curves of the 2nd cycle and b) charge capacity values for anode materials based on MoS_2 with 150 μm coating thickness at 0.1 A g^{-1}.

While $MoS_{cond\text{-}CB\text{-}150}$ material shows the most promising specific capacity value, its decay presents an opportunity to study the evolution of the processes with more scrutiny. For this, we have prepared MoS_2 anodes with PEDOT:PSS/CMC binder in a 20 µm to 300 µm range of coating thickness providing 0.07 mg cm^{-2} to 2.4 mg cm^{-2} mass loading.

We analyzed the ratios of capacities obtained from each plateau of the GCD curves (Figure 3) to study the relative contribution of each process into total capacity (Table 2). We assign the discharge plateaus to the processes accordingly: D_1 is the reduction of sulfur and polysulfides (Eq. 3), D_2 is lithium ions intercalation to form Li_xMoS_2 (Eq. 1), and D_3 is the plateau for MoS_2 conversion to metallic molybdenum and Li_2S (Eq. 2), that is highly likely interspersed with the process of SEI formation. On oxidation, charge plateau C_1 is the process of sulfur formation, with the rest of the GCDs being difficult to assign to specific processes. Comparing the GCD curves of the materials at various cycles allowed us to see the evolution of plateaus corresponding to these processes. The values of capacities are in reasonable agreement with theoretical ones, and the general trend of capacity fading goes as expected.

Consistently with the low current in CVs and poorly resolved plateaus on GCDs, MoS_{cond} demonstrates the lowest stability and most difficult assessment of the interval of capacities related to certain electrode processes. The process of Li^+ ions intercalation at ~1.1 V yields only 51 mA h g^{-1} in the 2nd cycle (contributing 14% of total capacity), and this plateau is hardly distinguishable in the 5th cycle already. The capacity related to sulfur-sulfides conversion (~1.9 V on reduction, and ~2.3 V on oxidation) also has low efficiency. On charge, only a quarter of total capacity may be assigned to Li_2S to S conversion.

As the resolution of the plateaus drops dramatically over the presented cycles, it becomes unclear, which process is responsible for capacity values over long cycling procedures. These values are approaching ca. 150 mA h g^{-1} by the 100th cycle for all samples of this thickness, regardless of the selected binder. This asymptotic behavior of MoS_2 long-term capacity has been reported in similar conditions [22,54].

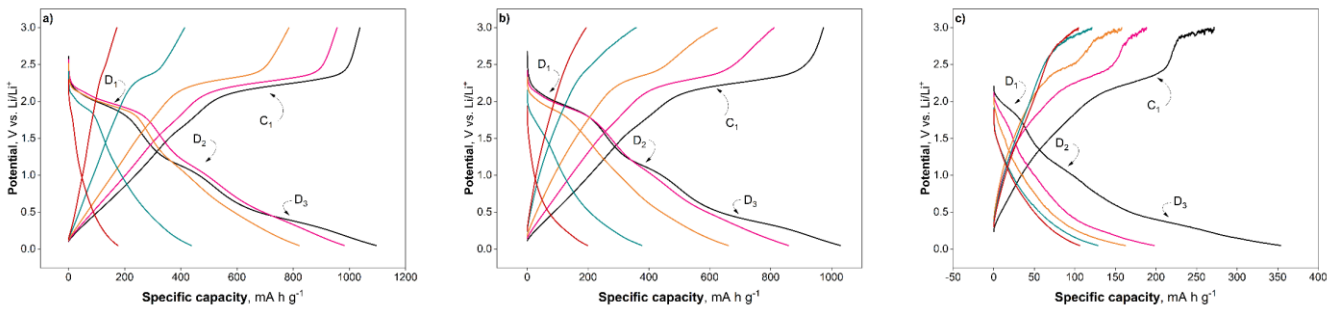

Figure 3. GCD curves of 2nd, 5th, 10th, 20th and 40th cycles for a) $MoS_{cond\text{-}CB\text{-}150}$, b) MoS_{PVDF}, c) MoS_{cond} samples at 0.1 A g^{-1}.

Higher initial specific capacity and best resolution of redox peaks on CVs, indicating better charge transfer properties, make samples with PEDOT:PSS/CMC optimal candidates for further studies of electrode thickness effects.

Table 2. Capacities of individual cycles; estimated capacities of the processes occurring in each charge and discharge; and relations between the capacities of separate electrochemical processes and total capacities, depending on the cycle number and electrode composition. All capacities (Q, C, and D values) are in mA h g^{-1}.

MoS_{PVDF}										
N	Q_D	D_1	D_1/Q_D	D_2	D_2/Q_D	D_3	D_3/Q_D	Q_C	C_1	C_1/Q_C
2	1030	186	18%	140	14%	248	24%	973	386	40%
5	860	154	18%	101	12%	322	37%	811	241	30%
10	660	113	17%	-	-	249	38%	624	147	24%
20	380	20	5%	-	-	181	48%	358	35	10%
40	200	-	-	-	-	125	63%	194	-	-
	$MoS_{cond\text{-}CB\text{-}150}$									
N	Q_D	D_1	D_1/Q_D	D_2	D_2/Q_D	D_3	D_3/Q_D	Q_C	C_1	C_1/Q_C
2	1095	174	16%	159	15%	287	26%	1037	447	43%
5	982	252	26%	123	13%	205	21%	956	403	42%
10	820	216	26%	72	9%	160	20%	784	315	40%
20	437	88	20%	-	-	116	27%	414	110	27%
40	175	11	6%	-	-	-	-	172	20	12%
MoS_{cond}										
N	Q_D	D_1	D_1/Q_D	D_2	D_2/Q_D	D_3	D_3/Q_D	Q_C	C_1	C_1/Q_C
2	354	26	7%	51	14%	85	24%	271	73	27%
5	198	11	6%	-	-	42	21%	188	55	29%
10	162	-	-	-	-	-	-	157	39	25%

3.2. Anode thickness effects on electrochemical properties

The dependence of the discussed processes on thickness is peculiar, as seen from CVs of the 5th cycle for $MoS_{cond\text{-}CB\text{-}20}$, $MoS_{cond\text{-}CB\text{-}70}$, $MoS_{cond\text{-}CB\text{-}100}$, and $MoS_{cond\text{-}CB\text{-}250}$ electrodes (**Figure 4**a). The peaks at ~2.2 V indicate lithium sulfide oxidation to sulfur, and peak-to-peak separation increases along with thickness, which is expected due to impeded diffusion and increase of internal ohmic resistance in the bulk of the material [55]. However, separation of peak potentials in Figure 4a and positions of plateaus in Figure 4b do not support the suggestion of increased ohmic resistance, because the largest peak separation is observed for $MoS_{cond\text{-}CB\text{-}250}$ electrodes with lower current density. We thus attribute peak separation to the increase of resistance towards lithium ions diffusion.

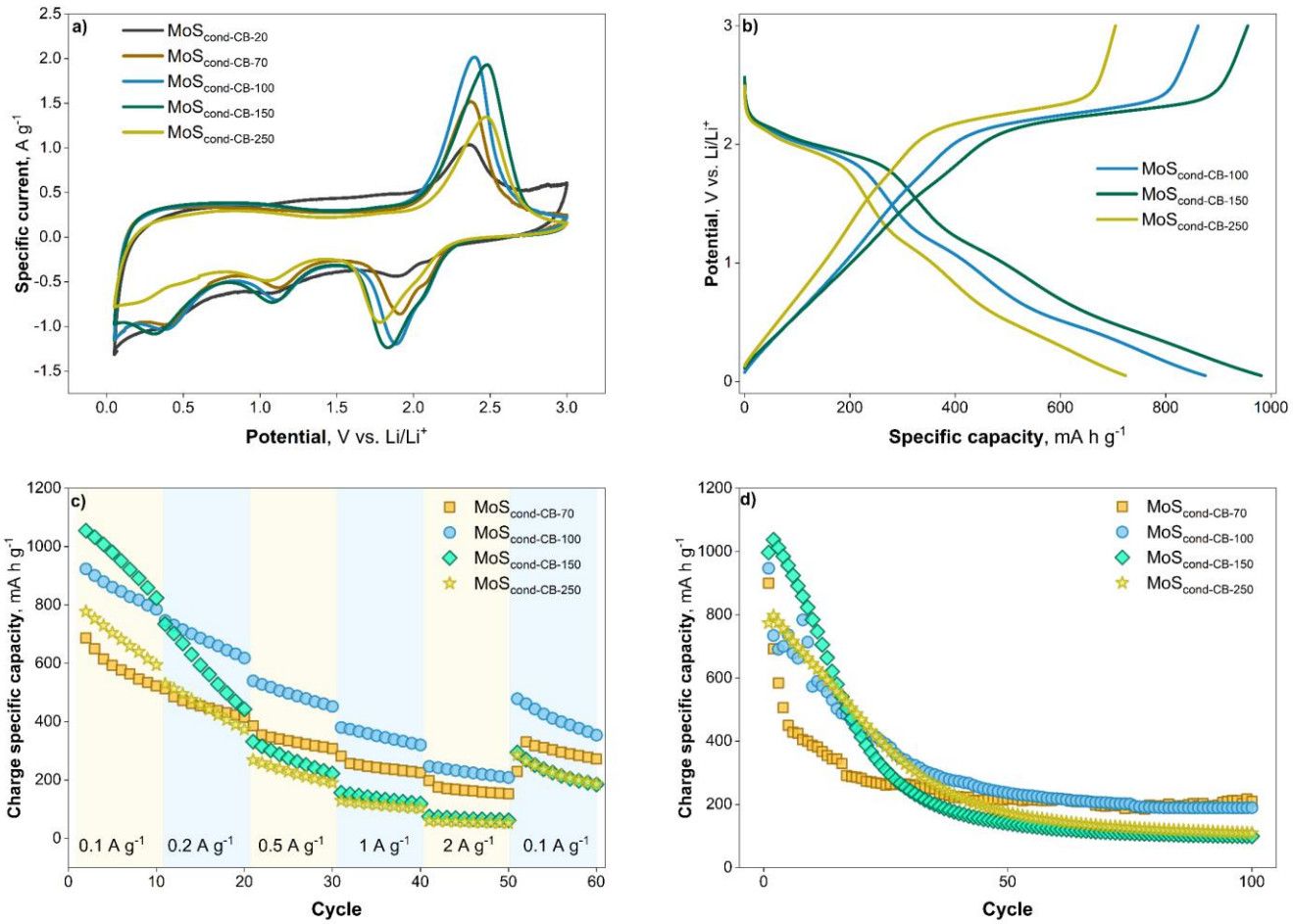

Figure 4. a) Cyclic voltammograms of the 5th cycle at 0.5 mV s^{-1}, b) galvanostatic charge-discharge curves on the 5th cycle at 0.1 A g^{-1}, c) charge rate capability, and d) charge cyclic stability at 0.1 A g^{-1} of MoS_2-based materials with different densities.

It was surprising that the electrodes with the lowest thickness have lower capacity than those with an average one, $MoS_{cond\text{-}CB\text{-}100}$. This is contrary to the expected performance of the electrodes with low mass loading, as it should provide an advantage of high utilization ratio of active substances, contributing to total specific capacity. Such behavior implies that the benefits of increased surface availability are overpassed by the arising drawbacks. It seems that in thinner electrodes more surface is exposed to the electrolyte, and there is no sufficient bulk of the material to hold polysulfides and prevent them from dissolution. This is especially true for $MoS_{cond\text{-}CB\text{-}20}$ electrodes, where the highest current densities are observed in the 2.7 V to 3.0 V area, with a hint of a rising peak.

Notably, the main oxidation peak does not exclusively represent Li_2S to S oxidation. Cycling the electrode in narrowed potential range showed (Figure 5a) that while the reduction peak at ~1.8 V remains of the same intensity for potential ranges of (0.9—3.0) V and (1.3—3.0) V, the current of oxidation peak at ~2.2 V drops. This means that the main oxidation peak is a superposition of peaks responsible for multiple processes. It may also mean that deep discharge increases the availability of Li_2S (and higher polysulfides). Additionally, limiting the potential by excluding the area of suggested SEI formation and

metallic Mo generation, i.e., cycling the cell in 0.6 V to 3.0 V, does not contribute to an increase of cyclic stability, yet the oxidation peak loses 19% of charge (calculated from the area) upon reducing the potential range (Figure 5b).

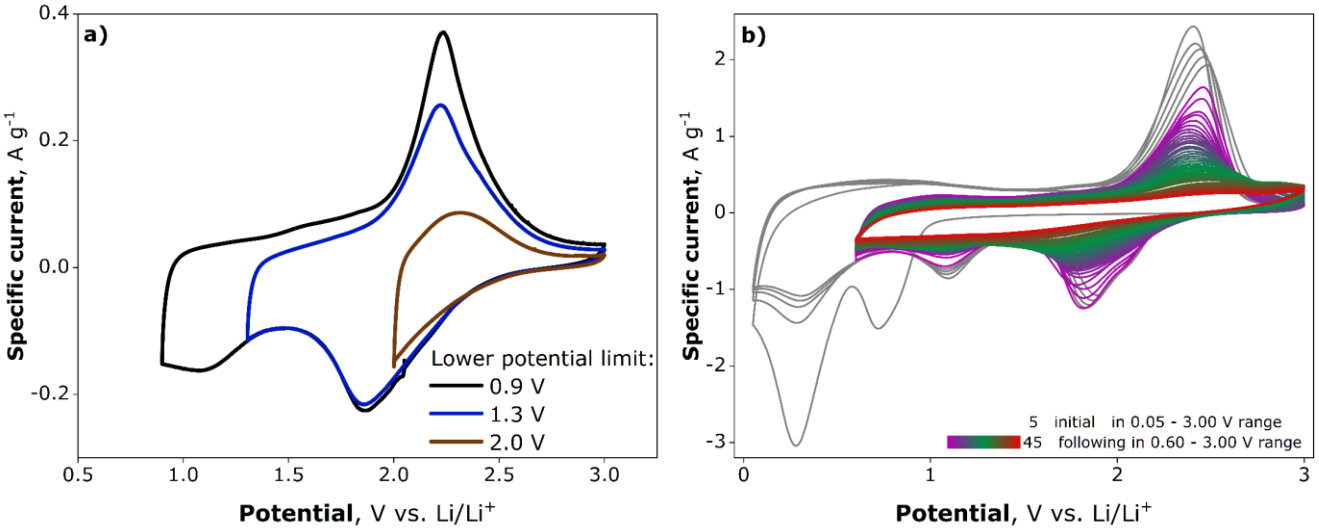

Figure 5. Cyclic voltammograms of $MoS_{cond\text{-}CB\text{-}50}$ sample in various potential ranges at 0.5 mV s^{-1} (a) and cyclic voltammograms evolution over 45 cycles for $MoS_{cond\text{-}CB\text{-}150}$ sample upon limiting the potential range at 0.5 mV s^{-1} (b).

As the lower-thickness materials seem to be susceptible to unwanted processes decreasing their activity, in Figure 4b galvanostatic charge-discharge curves are presented for materials with higher loading. The set of plateaus roughly corresponds to the earlier observed set of peaks for these materials. Namely, the discharge plateau at ~2.0 V indicates S reduction to Li_2S, followed by Li intercalation to form Li_xMoS_2 into the remaining MoS_2 at ~1.1 V. In the lower potentials area (<0.6 V), multiple processes related to SEI reactions and metallic Mo formation occur. In the charge curve, only one distinct plateau is observed centered at ~2.25 V, yet it contributes up to ~45% of total capacity, meaning that several processes are interspersed here. The remainder of oxidation capacity is mostly gained from 0.05 V to ~2.0 V area with a near-constant slope, which is usually associated with non-faradaic processes, such as interfacial lithium storage [56]. These processes are located at similar potential values for all samples, which means that the polarization of electrodes with different loadings barely changes. This indicates that for the low current density (0.1 A g^{-1}) the utilization of available active substance is equivalent for all samples after several GCD cycles. Normalizing the curves to state-of-charge coordinates results in their overlapping.

The rate capability of the samples data is presented in Figure 4c. The initial capacity at 0.1 A g^{-1} is highest for $MoS_{cond\text{-}CB\text{-}150}$ sample, 1055 mA h g^{-1}. For the rest of the samples, the initial capacities are 924 mA h g^{-1} for $MoS_{cond\text{-}CB\text{-}100}$, and 777 mA h g^{-1} for $MoS_{cond\text{-}CB\text{-}250}$. We must explicitly state that the capacity of 687 mA h g^{-1} was obtained for the $MoS_{cond\text{-}CB\text{-}70}$ sample when the upper potential was limited at 2.6 V. This was done because the side processes in the lower-thickness materials prevailed over

normal recharging processes in the (2.6–3.0) V range. Interestingly, the noisy upturned (2.6–3.0) V area in the CV (Figure 4a) of $MoS_{cond\text{-}CB\text{-}20}$ may even indicate gas evolution. This is a parasitic process that only occurs at low mass loadings, and may be linked to the catalytic activity of MoS_2 edge sites [57], which became explicitly available in thinner samples Regardless of the exact nature of the processes limiting the performance of lower-thickness electrodes, this is additional support for the need to find a compromise between higher charge transfer resistance in thicker electrodes and increased side processes activity in thinner ones. As the CV peaks and GCD plateaus for lithium sulfides conversion to sulfur occur at ca. (2.4–2.5) V, it should not have limited the main redox processes significantly. Another observation is that all the obtained values are higher than the theoretical capacity of MoS_2, which confirms earlier reports on additional capacity input from Li_2S/S redox pair and the probability of contribution of non-faradaic processes. The high initial capacity of the $MoS_{cond\text{-}CB\text{-}150}$ sample does not translate to its rate capability. At 2 A g^{-1}, only 9% of the value at 0.1 A $g^{-1}$is retained for $MoS_{cond\text{-}CB\text{-}150}$, 32% for $MoS_{cond\text{-}CB\text{-}100}$, 10% for $MoS_{cond\text{-}CB\text{-}250}$, and 38% for $MoS_{cond\text{-}CB\text{-}70}$. Again, when estimating the value for $MoS_{cond\text{-}CB\text{-}70}$, it should be considered that the upper voltage was limited. This seems to increase the rate capability while simultaneously decreasing total capacity. The omitted potentials area is crucial for full electrode material utilization, as coulombic efficiency is low in the case of the limited potentials range. The side processes area was not cut off in the case of $MoS_{cond\text{-}CB\text{-}100}$, and this seems to contribute to abnormally increased coulombic efficiency, while samples with 150 μm and 250 μm thickness start with ~97% efficiency, which stabilizes as cycling continues. We also observed a rise of polarization upon the increase of current density, and thicker samples were more prone to this effect, with ΔE increasing from 0.41 V for $MoS_{cond\text{-}CB\text{-}100}$ to 0.64 V for $MoS_{cond\text{-}CB\text{-}250}$. The resolution of plateaus is lower at 2 A g^{-1}, and it becomes difficult to determine Δ*E*. The obtained capacity values and their connection to the thickness of the electrode indicate that conditions for testing battery electrode materials should be intricately constructed to make use of their full capability.

Similar to rate capability, cyclic stability (Figure 4d) is highest for the $MoS_{cond\text{-}CB\text{-}70}$ sample with limited voltage. Here, 23% of the initial value is retained after 100 cycles at 0.1 A g^{-1}. It is followed by 14% for $MoS_{cond\text{-}CB\text{-}250}$, and 10% for $MoS_{cond\text{-}CB\text{-}150}$. $MoS_{cond\text{-}CB\text{-}100}$ retains 20% of the initial capacity, which is the highest for the samples with full cycling voltage. The fast rate of decay is inherent in non-nanostructured MoS_2 [22,29,58], yet the additional dependence of cycle life on the thickness and mass loading is worth considering for novel materials.

The capacity value in the late cycles is usually 108±8 mA h g^{-1}, with notable exceptions of lower-thickness samples still providing ca. (190–210) mA h g^{-1} by the 100^{th} cycle. This is an interesting trend, as it may be related to the reversible processes occurring with the remainder of active material under the assumption that all initially present MoS_2 has been converted. Considering that sulfur takes up 40% of the total active material (MoS_2) mass and presuming that only the $Li_2S \rightleftarrows S$ process remains in the later cycles, this means that the actual specific capacity values per sulfur mass are 270±8 mA h g^{-1} for thicker electrodes and up to 525 mA h g^{-1} for $MoS_{cond\text{-}CB\text{-}100}$.

Electrochemical properties of anodes prepared using bulk molybdenum disulfide and similar materials are presented in Table 3. The comparison shows that conductive PEDOT:PSS/CMC binder is beneficial for the capacity of our material, yet stability should be retained in other manner, such as manufacturing composites of MoS_2 with graphene. The unstable behavior of unmodified MoS_2 is

invariable in most literature data. This shows that further studies should focus on increasing the stability of the material to reach 95%–100% capacity retention over at least 100 cycles, while the conductive binder might be able to provide increased capacity and material availability during recharging process.

Table 3. Electrochemical parameters of similar anode materials reported in the literature.

Material	Specific capacity at 100 mA g^{-1}, mA h g^{-1}	Capacity retention, %/cycles
MoS_2 [59]	~890	~6%/100
MoS_2/C [59]	~1040	~50%/100
MoS_2 [60]	1031	95%/100
C@MoS_2@NC [61]	747	54%/100
MoS_2/Cu [62]	1351	50%/200
MoS_2 [62]	873	12%/200
MoS_2/graphene [22]	825	100%/120
MoS_2 [22]	166	<20%/120
MoS_2 [63]	~700	~50%/50
Graphene-like MoS_2 with amorphous carbon [63]	~900	~100%/100
MoS_2 with PEDOT:PSS/CMC binder (this work)	1040	10%/100

Electrochemical impedance spectroscopy measurements were employed to further investigate the electrochemical response of different electrodes during cycling. EIS allows us to look closer at the processes involved in the transport of charge carriers. We have recorded EIS spectra to compare both the effect of the used binder (Figure 6a), and of the thickness of electrodes with conductive PEDOT:PSS/CMC binder with carbon black (Figure 6b). We determined the influence of mass loading and electrode composition on electrochemical performance by measuring EIS spectra in two-electrode cell configuration. This approach assumed that contribution of Li/Li^+ reaction on the negative electrode can be neglected. Therefore, the total impedance of the cell was interpreted as the impedance of the MoS_2-based electrode. On initial cycles (for EIS measurements after 3rd CV cycle), the obtained EIS spectra in Nyquist plots consist of two characteristic parts: a well-defined semicircle at high frequencies (100 kHz to ~ (1–5) Hz), and an inclined line at low frequencies (~ (1–5) Hz to 0.01 Hz). The semicircle is preceded by solvent resistance R_s, which was 4 Ω for all samples.

The obtained spectra were fitted using the equivalent circuits previously suggested for MoS_2-based materials (see embedded scheme in Figure 6a) [56,64–66]. The presented circuit provided the most adequate fit to the experimental data in the high-frequency region. The two RC-parallel elements in series correspond to the slightly distorted semicircle. As the semicircle is depressed, constant phase

elements (CPE) provide a better fit than capacitors. The processes and equivalent circuit elements were partially matched using available literature on conversion type materials [67]. Attribution of R_1 and R_2 to the processes in the cell may vary, yet we may assume that R_1 is charge transfer resistance, in parallel with double-layer capacitance, here represented by CPE_1. This means R_2 is the resistance of conversion reaction in the electrode material, which should be accompanied by chemical capacitance (probably Faradaic) CPE_2. CPE was included in place of capacitors to account for frequency-dependent capacitance caused by inhomogeneous bulk and surface composition of the electrode and its porosity. We also include the Z_w Warburg element to explain the slow diffusion of lithium ions in the bulk of the material, which is represented by a short section of line with a slope of 45° in the mid-frequency region. One would expect Warburg impedance to be visible in the mid-to-high frequencies region, followed by a low-frequency capacity response. However, the emergence of new phases (i.e., sulfur, lithium sulfide, and polysulfides) affects the impedance spectra in such a way as to make it difficult to distinguish Warburg impedance in higher frequencies area.

Before recording impedance spectra, 3 consecutive CV cycles of the cells were recorded at 0.1 mV s^{-1} in 0.05 V to 3.00 V, starting and ending with the open-circuit potential value. From the spectra for electrodes with various binders (Figure 6a), we can immediately conclude that conductive PEDOT:PSS/CMC binder with carbon black (sample $MoS_{cond\text{-}CB\text{-}150}$) provides the most beneficial charge transfer properties and minimal resistance of chemical reaction. As we aimed to use the equivalent scheme that allows for better comparison of samples (rather than providing a separate scheme for each case), there are deviations from optimal fit. The following discussion mostly relies on obtained resistance values, the general trend of which is valid for schemes suitable for fitting spectra with two semicircles. The values obtained from the fitted equivalent schemes are presented in Table 4. Here, the values of both R_1 and R_2 are much higher for MoS_{PVDF} and MoS_{cond} samples, than for $MoS_{cond\text{-}CB\text{-}150}$. The 294 Ω and 1650 Ω values for the MoS_{cond} sample indicate clearly that carbon black is a necessity even with conducting polymer. R_1 and R_2 values for MoS_{PVDF} are approximately 4 times higher than the values for $MoS_{cond\text{-}CB\text{-}150}$, which means better availability of the material with conducting polymer to both redox and charge transfer processes. Conductive binder also brings the material closer to composites with carbon materials in terms of reduced charge transfer resistance [46,56].

Table 4. The values of the parameters for different materials studied using electrochemical impedance spectroscopy near open-circuit potential obtained using an equivalent circuit presented in Figure 6.

	MoS_{PVDF}	MoS_{cond}	$MoS_{cond\text{-}CB\text{-}70}$	$MoS_{cond\text{-}CB\text{-}100}$	$MoS_{cond\text{-}CB\text{-}150}$	$MoS_{cond\text{-}CB\text{-}250}$
m, mg	2.5	2.7	0.76	1.0	1.4	3.1
R_1, Ω	234±2	294±3	58.4±0.2	58.9±0.1	48.6±0.4	21.7±0.2
R_2, Ω	220±10	1650±50	350±20	45±1	60±10	150±20
χ^2	0.03	0.03	0.009	0.003	0.03	0.05
r_1, Ω mg	590	800	44	59	68	67
r_2, Ω mg	550	4500	270	46	83	465

Absolute impedance values for samples with different thicknesses (Figure 6b) do not follow a specific order, which highlights the necessity of surface-normalization of these values. We appeal to the method of mass-normalization of impedance in the assumption that surface area is proportional to the mass loading of electrodes [41]. For electrodes with thickness varied from 100 µm to 250 µm the diameters of semicircles decrease along with the increase of MoS_2 mass loading. Assuming the main contribution to interfacial charge transfer resistance arises from the charge transfer resistance on electrode material-electrolyte interface, the increase of the real surface area of active particles due to higher mass loading should lead to a decrease of R_1 accordingly.

Thus, we obtain r_1 values by multiplying R_1 by the mass of respective electrode loadings. The validity of the calculation of normalized values is supported by the sequence of r_1 values presented in Table 4 (4th row). These values moderately increase along with the thickness.

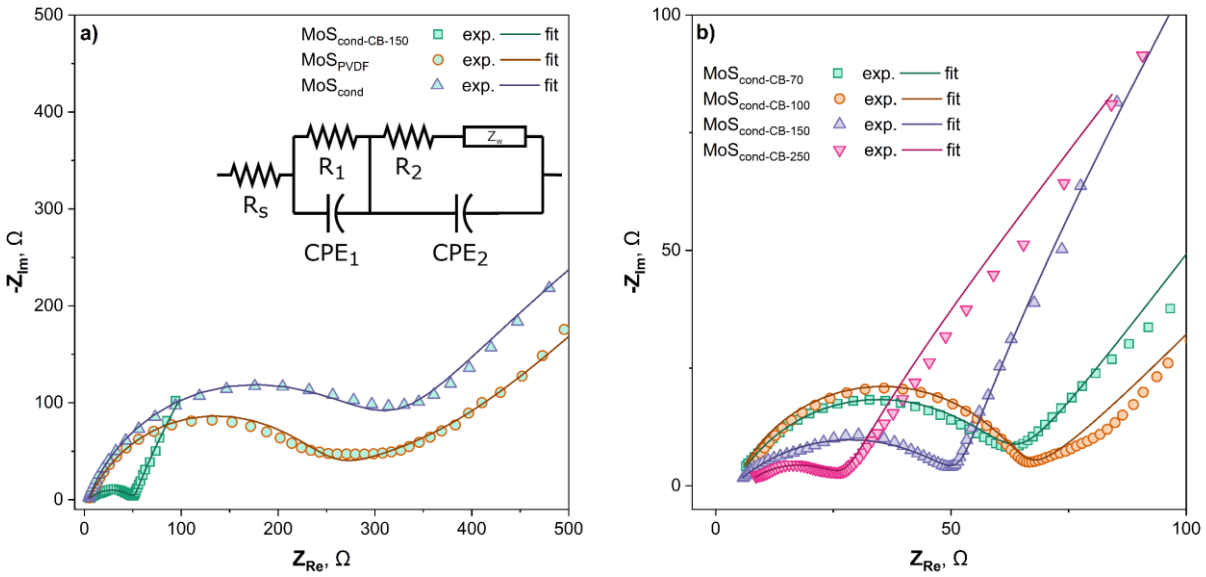

Figure 6. Electrochemical impedance spectra of half-cells with materials with various binders (a) and half-cells with materials with conductive binder PEDOT:PSS/CMC and carbon black with various thicknesses.

In contrast, a similar procedure for R_2 values does not produce a result fitting with the mass normalization concept. The r_2 values increase drastically (by a factor of 5.6, and by a factor of 2.5 for non-normalized R_1 values) when the thickness increases from 100 µm to 250 µm. Such increase may mean that in denser and thicker samples the availability of material for chemical reactions decreases, as fewer particles in the depth of material are available for interactions with lithium. This might be additionally complicated by the low conductivity of sulfur and Li_2S, and the low mobility of polysulfides. The behavior of the $MoS_{cond\text{-}CB\text{-}70}$ sample is slightly different in this regard. The charge transfer resistance r_1 is the lowest here, which is justified by low thickness and thus greater access of electrolyte to the active particles. However, r_2 value does not follow the trend of decreasing with lower thickness. We

suppose that the cause of such an exception is a much higher disconnect between MoS_2 particles, which cannot interact with each other and thus are forced to act like individual localized redox sites, rather than homogenous material. All spectra were recorded at open-circuit voltage after 3 CV cycles. After recording impedance spectra, the samples were cycled for additional 50 cycles at 100 mA g^{-1} (to reach the low-capacity state as per cycle life plots (Figure 2b, Figure 4d)). The obtained spectra and their comparison with initial (Figure 7) clearly show that the mechanism of degradation cannot only be described by EIS measurements, as there is no clear tendency observed for the dependence of spectra on binder and electrode thickness. These data warrant future studies to discern various effects, such as mass loss (i.e., dissolution), polysulfides formation, full replacement of initial MoS_2 material with S/Li_2S pair, etc.

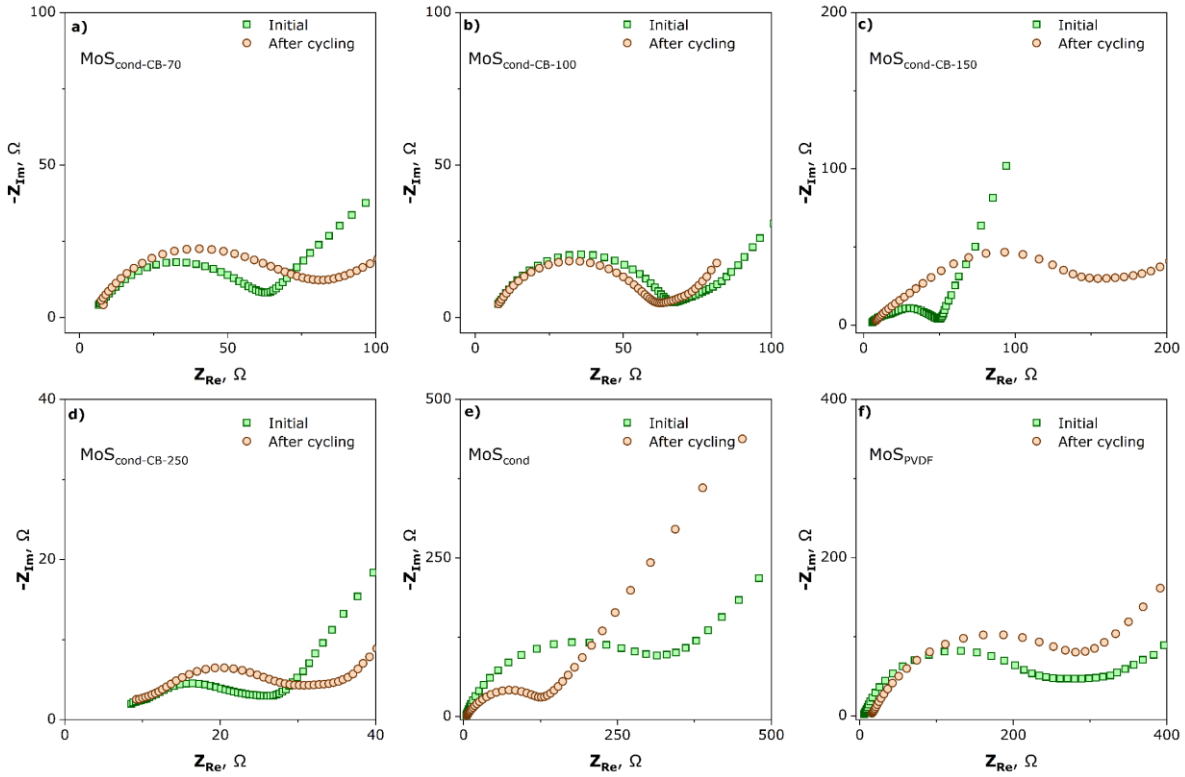

Figure 7. Electrochemical impedance spectra of MoS_2-based electrodes before and after 50 charge-discharge cycles at 0.1 A g^{-1} depending on thickness for PEDOT:PSS/CMC binder and carbon black (a-d), for MoS_{cond} (e), and MoS_{PVDF} (f).

The obtained results are helpful in studying the systems with conversion type electrodes, especially MoS_2-based ones, and can be useful in determining optimal mass loadings of such electrodes.

3.3. Morphological and structural analyses

3.3.1. Scanning electron microscopy

SEM images of post-mortem samples with different binders are useful for understanding the difference in electrochemical behavior. We believe that the MoS_{PVDF} sample (Figure 8a,c) has lower susceptibility to dissolution and is more prone to the formation of polysulfides than analogous $MoS_{cond\text{-}CB\text{-}150}$ (Figure 8b,d) primarily due to particles distribution in the polymer binder. Although both samples are amorphous, there is a difference in MoS_2 platelets exposure. In the case of PVDF binder, MoS_2 particles are clearly visible protruding through the coating. Such heterogeneity is noticeable both before and after cycling. This may contribute to sulfides and polysulfides dissolution upon recharging, as there is no polymer structure to capture them.

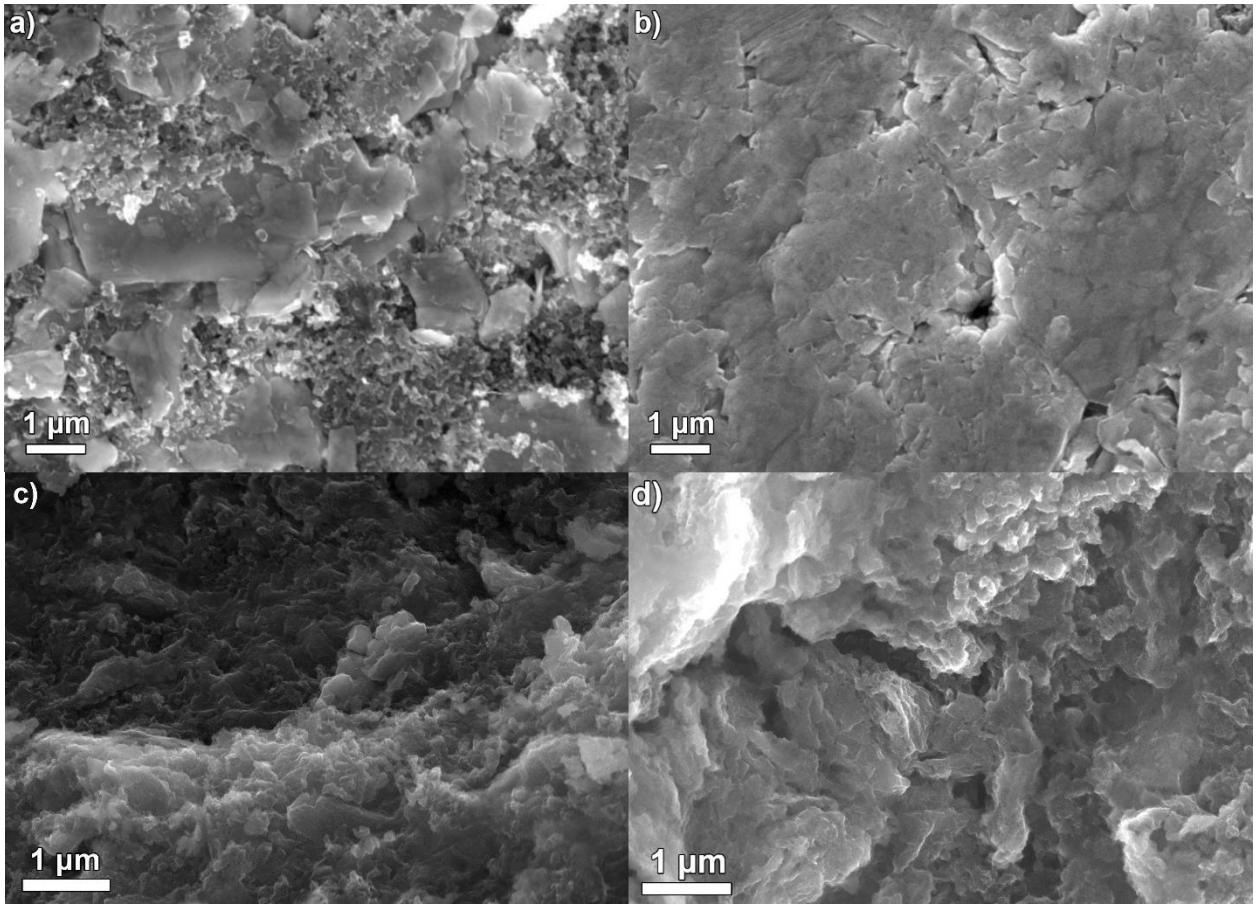

Figure 8. SEM images of (a, c) MoS_{PVDF}, and (b, d) $MoS_{cond\text{-}CB\text{-}150}$ electrode samples before assembly (a, b) and after extraction from half-cells after cycle life studies (c, d).

On the contrary, PEDOT:PSS/CMC binder fully coats MoS_2 and may prevent it from dissolving, as well as keep the structure more stable. Comparing images in Figure 8b and Figure 8d also shows that the initially smooth surface of the coating with a conductive binder is disturbed upon multiple recharging cycles, resulting in a more open porous structure. While porosity is usually associated with better

availability of the surface, it might also prevent polysulfides confinement, which is a plausible reason for the instability of electrodes even with PEDOT:PSS/CMC binder.

3.3.2. High-resolution X-ray diffraction

Ex situ HR-XRD studies of postmortem samples provide a spectrum (Figure 9a) that allows determining the main phase of the material after cycling and extraction from the cell. Please note that in this case we used a sample with higher loading, $MoS_{cond\text{-}CB\text{-}300}$. This is due to the inability of HR-XRD to obtain easily interpretable spectra for samples with lower loadings. Wider spectral peaks in the case of thinner coatings usually indicate structures and crystallites of nanoscale sizes [68]. This may mean that the phase transformations and redox reactions within the samples produce particles that are different from the initial ones at least in size.

Should MoS_2 have been preserved in the sample, it would remain stable, though other products of electrochemical reactions may have interacted with water and oxygen in the air. This is not the case here, as the XRD spectrum (Figure 9a) only allows to identify (with exception of copper peak belonging to current collector) Li_2MoO_4. As there are no sources of oxygen in the sealed coin cells, this compound is evident to form after electrode extraction. Its formation requires molybdenum to be in some form capable of forming bonds with air components, specifically with water [69]. Usually, metallic Mo forms MoO_3 only when exposed to air at high temperatures [70], yet its nanoparticle form may contribute to its oxidation at normal temperature. There is no signal of either sulfur or sulfides, likely due to their amorphous nature. For reference, the XRD spectrum of the initial MoS_2 powder is also included (Figure 9b).

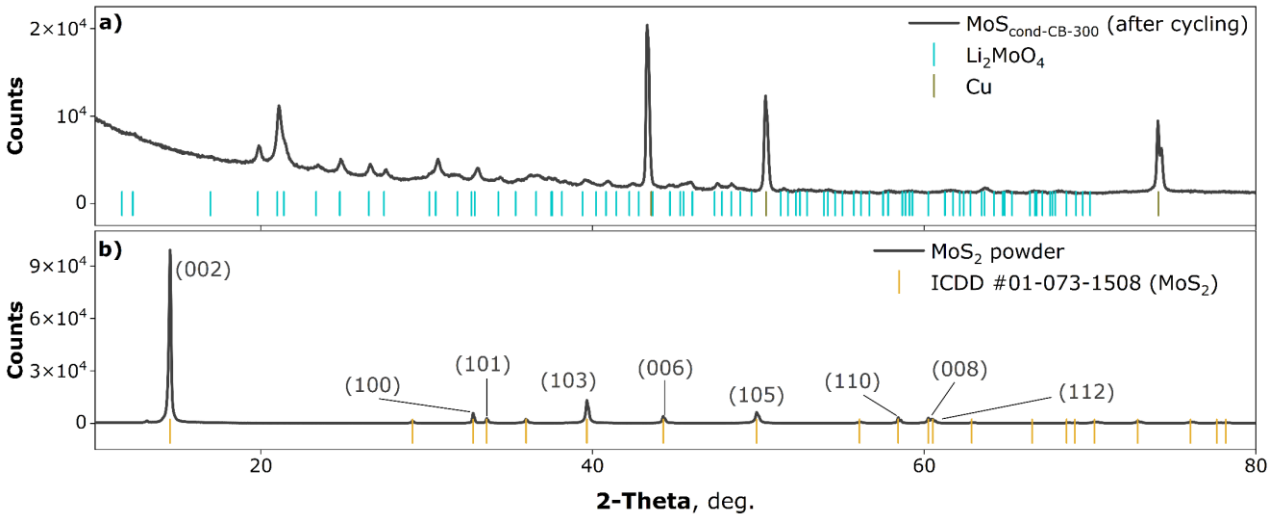

Figure 9. XRD spectrum of $MoS_{cond\text{-}CB\text{-}300}$ extracted from half-cell after cycle life studies (a) and XRD spectrum of MoS_2 commercial powder (Aldrich, 90 nm) used in this work (b).

3.3.3. X-ray photoelectron spectroscopy

The XPS spectra of MoS_{PVDF} and $MoS_{cond\text{-}CB\text{-}150}$ electrodes recorded after extraction from cycled cells (Figure 10) support the conclusions drawn from HR-XRD analysis. In both cases, the Mo3d spectra (Figure 10a) contain a peak at ~232 eV (Mo^{4+} $3d_{3/2}$), yet the peak at ~229 eV associated with Mo-S bonding of 2H-MoS_2 [71], is missing. This may mean that Mo exists in oxide or lithiated oxide Li_2MoO_4 [72], which is supported by the presence of the peak at ~235 eV attributed to Mo^{6+} [73]. S2p spectra (Figure 10b) contain a peak at ~162 eV, which may indicate the existence of MoS_2 [74], yet this peak may also be indicative of Li_2S or Li_2S_2 [75]. The (168.5–168.7) eV peak indicates the presence of sulfates, produced due to material oxidation [76].

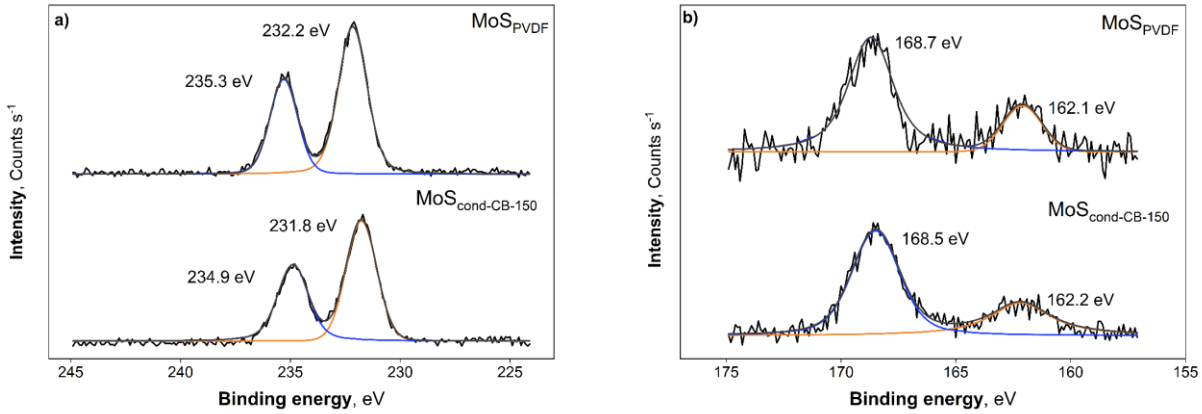

Figure 10. XPS spectra of MoS_{PVDF} and $MoS_{cond\text{-}CB\text{-}150}$ electrodes extracted from CR2032 cells after 100 charge-discharge cycles at 0.1 A g^{-1}. a) Mo3d, b) S2p

As a result, presented spectral studies indicate intense conversion of initial MoS_2 into (likely lithiated) oxides and sulfates. While it is unlikely (in absence of oxygen) for these to appear during cycling, the processes that occurred in the cell made the products prone to oxidation upon cell disassembly.

4. CONCLUSIONS

In summary, novel results of systematic investigation of the effect of the thickness of MoS_2-based electrodes with PEDOT:PSS/CMC conductive binder (varied from 20 μm to 250 μm) on the functional properties of assembled coin cells has been presented and discussed. Remarkably, there is an optimal middle thickness that allows finding a compromise between the disadvantages of both thin and thick electrodes. The highest initial specific capacitance of MoS_2/PEDOT:PSS/CMC electrodes of ca. 1055 mA h g^{-1} at 0.1 A g^{-1} was observed at the moderate thickness of the electrode layer (150 μm). Cell polarization rises slightly as current density and thickness increase.

Additionally, the electrode composition was optimized by using a water-soluble conductive binder PEDOT:PSS/CMC. The initial capacity values of the $MoS_{cond\text{-}CB\text{-}150}$ sample (1040 mA h g^{-1}) were superior to other investigated samples: MoS_{PVDF}, and MoS_{cond} with initial capacities of 970 mA h g^{-1} and 410 mA h g^{-1}, respectively. This means that the replacement of a standard binder with a conductive one provides some advantage. However, the experimental results showed that capacity fading does not significantly vary neither with the thickness of MoS_2-based electrodes nor with various binders, which means that more radical approaches to the structuring of electrodes should be employed in the future. EIS kinetic parameters were obtained and analyzed. The electrode materials prepared with conductive binder show a 4-fold decrease in charge transfer resistance in assembled half-cells, compared to materials with conventional PVDF binder. The benefit is likely due to better material coating and facilitated charge transfer. Meanwhile, the lowest charge transfer resistance and degradation of electrode performance are observed for samples with medium (100 μm to 150 μm) electrode thickness. The causes for this effect are multifold: particles distribution in the conductive binder and their interconnection, as well as conversion reactions occurring in the material during cycling all contribute to performance. There is a middle ground between the excessive dissolution of the surface material in thinner electrodes and low access of the electrolyte to the material in thicker ones. This work provides more information on processes that occur in MoS_2 anodes and may help in further studies of materials for both lithium-ion and lithium-sulfur batteries.

ACKNOWLEDGEMENTS

The reported study was funded by Russian Foundation for Basic Research, project number 20-33-90143. The authors would like to thank Centre for X-ray Diffraction Studies, Centre for Physical Methods of Surface Investigation, and Interdisciplinary Resource Centre for Nanotechnology of Research Park of St. Petersburg State University.

References

1. T. Stephenson, Z. Li, B. Olsen, D. Mitlin, *Energy Environ. Sci.*, 7 (2014) 209–231.
2. Y. Wu, Y. Yu, *Energy Storage Mater.*, 16 (2019) 323–343.
3. R. Zhang, Y. Qin, P. Liu, C. Jia, Y. Tang, H. Wang, *ChemSusChem*, 13 (2020) 1354–1365.
4. B. Schönfeld, J.J. Huang, S.C. Moss, *Acta Crystallogr. Sect. B Struct. Sci.*, 39 (1983) 404–407.
5. L.F. Mattheiss, *Phys. Rev. B*, 8 (1973) 3719–3740.
6. G.K. Veerasubramani, M.-S. Park, G. Nagaraju, D.-W. Kim, *J. Mater. Chem. A*, 7 (2019) 24557–24568.
7. L. Gao, Q. Dong, S. Bai, S. Liang, C. Hu, J. Qiu, *ACS Sustain. Chem. Eng.*, 8 (2020) 9690–9697.
8. X. Gan, H. Zhao, D. Lei, P. Wang, *J. Catal.*, 391 (2020) 424–434.
9. Y. Liu, J. Chen, C. Xu, T. Yu, Z. Li, Z. Wei, L. Qian, Y. Wan, P. Yang, Z. Wang, S. Luo, H. Sun, *Electrochim. Acta*, 353 (2020) 136545.
10. Q. Zhu, C. Zhao, Y. Bian, C. Mao, H. Peng, G. Li, K. Chen, *Synth. Met.*, 235 (2018) 103–109.
11. J. Wu, J. Liu, J. Cui, S. Yao, M. Ihsan-Ul-Haq, N. Mubarak, E. Quattrocchi, F. Ciucci, J.-K. Kim, *J. Mater. Chem. A*, 8 (2020) 2114–2122.
12. C. Zhao, C. Yu, B. Qiu, S. Zhou, M. Zhang, H. Huang, B. Wang, J. Zhao, X. Sun, J. Qiu, *Adv. Mater.*, 30 (2018) 1702486.

13. Y. Cui, W. Liu, W. Feng, Y. Zhang, Y. Du, S. Liu, H. Wang, M. Chen, J. Zhou, *Adv. Funct. Mater.*, 30 (2020) 1908755.
14. Y.-H. Tan, F. Zhou, Z.-H. Huang, W.-T. Yao, T.-W. Zhang, H.-B. Yao, L.-L. Lu, S.-H. Yu, *ChemElectroChem*, 5 (2018) 995–995.
15. H. Li, Q. Yang, F. Mo, G. Liang, Z. Liu, Z. Tang, L. Ma, J. Liu, Z. Shi, C. Zhi, *Energy Storage Mater.*, 19 (2019) 94–101.
16. V.O. Koroteev, S.G. Stolyarova, A.A. Kotsun, E. Modin, A.A. Makarova, Y. Shubin, P.E. Plyusnin, A.V. Okotrub, L.G. Bulusheva, *Carbon N. Y.*, 173 (2021) 194–204.
17. Z. Li, A. Ottmann, Q. Sun, A.K. Kast, K. Wang, T. Zhang, H.-P. Meyer, C. Backes, C. Kübel, R.R. Schröder, J. Xiang, Y. Vaynzof, R. Klingeler, *J. Mater. Chem. A*, 7 (2019) 7553–7564.
18. G. Wang, J. Zhang, S. Yang, F. Wang, X. Zhuang, K. Müllen, X. Feng, *Adv. Energy Mater.*, 8 (2018) 1702254.
19. J. Wu, F. Ciucci, J. Kim, *Chem. – A Eur. J.*, 26 (2020) 6296–6319.
20. L. Wang, Q. Zhang, J. Zhu, X. Duan, Z. Xu, Y. Liu, H. Yang, B. Lu, *Energy Storage Mater.*, 16 (2019) 37–45.
21. S. Yu, M.J. Zachman, K. Kang, H. Gao, X. Huang, F.J. DiSalvo, J. Park, L.F. Kourkoutis, H.D. Abruña, *Adv. Energy Mater.*, 9 (2019) 1902773.
22. Y. Li, Z. Liu, X. Cheng, X. Liu, B. Zhang, D. Sun, R. Wang, Y. Zhang, *Energy Storage Mater.*, 9 (2017) 188–194.
23. T. Zhao, H. Shu, Z. Shen, H. Hu, J. Wang, X. Chen, *J. Phys. Chem. C*, 123 (2019) 2139–2146.
24. S. Parida, A. Mishra, J. Chen, J. Wang, A. Dobley, C.B. Carter, A.M. Dongare, *J. Am. Ceram. Soc.*, 103 (2020) 6603–6614.
25. M. Rana, S.A. Ahad, M. Li, B. Luo, L. Wang, I. Gentle, R. Knibbe, *Energy Storage Mater.*, 18 (2019) 289–310.
26. H.-E. Wang, X. Li, N. Qin, X. Zhao, H. Cheng, G. Cao, W. Zhang, *J. Mater. Chem. A*, 7 (2019) 12068–12074.
27. M. Wang, L. Fan, D. Tian, X. Wu, Y. Qiu, C. Zhao, B. Guan, Y. Wang, N. Zhang, K. Sun, *ACS Energy Lett.*, 3 (2018) 1627–1633.
28. A. Manthiram, Y. Fu, S.-H. Chung, C. Zu, Y.-S. Su, *Chem. Rev.*, 114 (2014) 11751–11787.
29. L. Zhang, D. Sun, J. Kang, J. Feng, H.A. Bechtel, L.W. Wang, E.J. Cairns, J. Guo, *Nano Lett.*, 18 (2018) 1466–1475.
30. C.-Y. Wei, P.-C. Lee, C.-W. Tsao, L.-H. Lee, D.-Y. Wang, C.-Y. Wen, *ACS Appl. Energy Mater.*, 3 (2020) 7066–7072.
31. G. Huang, *Int. J. Electrochem. Sci.*, 15 (2020) 5416–5429.
32. S. Xia, Y. Wang, Y. Liu, C. Wu, M. Wu, H. Zhang, *Chem. Eng. J.*, 332 (2018) 431–439.
33. X. Yu, J. Tang, K. Terabe, T. Sasaki, R. Gao, Y. Ito, K. Nakura, K. Asano, M. Suzuki, *Mater. Chem. Phys.*, 239 (2020) 121987.
34. W. Qin, Y. Li, Y. Teng, T. Qin, *J. Colloid Interface Sci.*, 512 (2018) 826–833.
35. P. Balaya, *Energy Environ. Sci.*, 1 (2008) 645.
36. K. Chang, W. Chen, *ACS Nano*, 5 (2011) 4720–4728.
37. R. Razaq, N. Zhang, Y. Xin, Q. Li, J. Wang, Z. Zhang, *ChemistrySelect*, 5 (2020) 7563–7570.
38. L. Yan, N. Luo, W. Kong, S. Luo, H. Wu, K. Jiang, Q. Li, S. Fan, W. Duan, J. Wang, *J. Power Sources*, 389 (2018) 169–177.
39. H. Zheng, J. Li, X. Song, G. Liu, V.S. Battaglia, *Electrochim. Acta*, 71 (2012) 258–265.
40. A.I. Volkov, S.N. Eliseeva, E.G. Tolstopjatova, V. V. Kondratiev, *J. Solid State Electrochem.*, 24 (2020) 1607–1614.
41. M.A. Kamenskii, S.N. Eliseeva, E.G. Tolstopjatova, A.I. Volkov, D.V. Zhuzhelskii, V.V. Kondratiev, *Electrochim. Acta*, 326 (2019) 134969.
42. J. Bai, B. Zhao, J. Zhou, J. Si, Z. Fang, K. Li, H. Ma, J. Dai, X. Zhu, Y. Sun, *Small*, 15 (2019) 1805420.

43. A.N. Enyashin, G. Seifert, *Comput. Theor. Chem.*, 999 (2012) 13–20.
44. Z. Zhu, Y. Tang, Z. Lv, J. Wei, Y. Zhang, R. Wang, W. Zhang, H. Xia, M. Ge, X. Chen, *Angew. Chemie Int. Ed.*, 57 (2018) 3656–3660.
45. C. Chai, H. Tan, X. Fan, K. Huang, *J. Alloys Compd.*, 820 (2020) 153144.
46. X. Zhou, Z. Wang, W. Chen, L. Ma, D. Chen, J.Y. Lee, *J. Power Sources*, 251 (2014) 264–268.
47. J. Wan, W. Bao, Y. Liu, J. Dai, F. Shen, L. Zhou, X. Cai, D. Urban, Y. Li, K. Jungjohann, M.S. Fuhrer, L. Hu, *Adv. Energy Mater.*, 5 (2015) 1401742.
48. S. Xue, S. Yao, M. Jing, L. Zhu, X. Shen, T. Li, Z. YiLiu, *Electrochim. Acta*, 299 (2019) 549–559.
49. Q. Wu, X. Zhou, J. Xu, F. Cao, C. Li, *J. Energy Chem.*, 38 (2019) 94–113.
50. K. Ma, H. Jiang, Y. Hu, C. Li, *Adv. Funct. Mater.*, 28 (2018) 1804306.
51. J. Lee, W. Choi, *J. Electrochem. Soc.*, 162 (2015) A935–A939.
52. S.A. Abbas, M.A. Ibrahem, L.-H. Hu, C.-N. Lin, J. Fang, K.M. Boopathi, P.-C. Wang, L.-J. Li, C.-W. Chu, *J. Mater. Chem. A*, 4 (2016) 9661–9669.
53. S. Ahn, T. Noguchi, T. Momma, H. Nara, T. Yokoshima, N. Togasaki, T. Osaka, *Chem. Phys. Lett.*, 749 (2020) 137426.
54. X. Luo, N. Li, X. Guo, K. Wu, *J. Solid State Chem.*, 296 (2021) 122020.
55. H. Gao, Q. Wu, Y. Hu, J.P. Zheng, K. Amine, Z. Chen, *J. Phys. Chem. Lett.*, 9 (2018) 5100–5104.
56. S. Gao, L. Yang, J. Shao, Q. Qu, Y. Wu, R. Holze, *J. Electrochem. Soc.*, 167 (2020) 100525.
57. U. Krishnan, M. Kaur, K. Singh, M. Kumar, A. Kumar, *Superlattices Microstruct.*, 128 (2019) 274–297.
58. J. Zhou, J. Qin, X. Zhang, C. Shi, E. Liu, J. Li, N. Zhao, C. He, *ACS Nano*, 9 (2015) 3837–3848.
59. D.A. Dinh, T.L. Nguyen, T.V. Cuong, K.S. Hui, T.H. Bui, S. Wu, K.N. Hui, *Energy and Fuels*, 35 (2021) 3459–3468.
60. Y.H. Zhang, R.H. Liu, L.J. Zhao, L.J. Xu, S.H. Luo, Q. Wang, X. Liu, *J. Electroanal. Chem.*, 873 (2020) 114428.
61. F. Wang, F. Li, L. Ma, M. Zheng, *Chem. - A Eur. J.*, 25 (2019) 14598–14603.
62. Y. Tian, X. Liu, X. Cao, D. Zhang, S. Xiao, X. Li, Z. Le, X. Li, H. Li, *Chem. Eng. J.*, 374 (2019) 429–436.
63. K. Chang, W. Chen, L. Ma, H. Li, H. Li, F. Huang, Z. Xu, Q. Zhang, J.Y. Lee, *J. Mater. Chem.*, 21 (2011) 6251–6257.
64. H. Zhao, H. Wu, J. Wu, J. Li, Y. Wang, Y. Zhang, H. Liu, *J. Colloid Interface Sci.*, 552 (2019) 554–562.
65. J. Wang, J. Liu, D. Chao, J. Yan, J. Lin, Z.X. Shen, *Adv. Mater.*, 26 (2014) 7162–7169.
66. Y. Lei, K. Fujisawa, F. Zhang, N. Briggs, A.R. Aref, Y.-T. Yeh, Z. Lin, J.A. Robinson, R. Rajagopalan, M. Terrones, *ACS Appl. Energy Mater.*, 2 (2019) 8625–8632.
67. N. Vicente, M. Haro, G. Garcia-Belmonte, *Chem. Commun.*, 54 (2018) 1025–1040.
68. C.F. Holder, R.E. Schaak, *ACS Nano*, 13 (2019) 7359–7365.
69. T. Quan, Y. Xu, M. Tovar, N. Goubard-Bretesché, Z. Li, Z. Kochovski, H. Kirmse, K. Skrodczky, S. Mei, H. Yu, D. Abou-Ras, M. Wagemaker, Y. Lu, *Batter. Supercaps*, 3 (2020) 747–756.
70. V. Madhavi, P. Kondaiah, S.S. Rayudu, O.M. Hussain, S. Uthanna, *Mater. Express*, 3 (2013) 135–143.
71. G. Eda, H. Yamaguchi, D. Voiry, T. Fujita, M. Chen, M. Chhowalla, *Nano Lett.*, 11 (2011) 5111–5116.
72. G. Seifert, J. Finster, H. Müller, *Chem. Phys. Lett.*, 75 (1980) 373–377.
73. L. Yang, W. Zhou, D. Hou, K. Zhou, G. Li, Z. Tang, L. Li, S. Chen, *Nanoscale*, 7 (2015) 5203–5208.
74. M.. Baker, R. Gilmore, C. Lenardi, W. Gissler, *Appl. Surf. Sci.*, 150 (1999) 255–262.

75. Y. Wu, T. Jin, T. Momma, T. Yokoshima, H. Nara, T. Osaka, *J. Power Sources*, 399 (2018) 287–293.
76. M. Liu, C. Zhang, J. Su, X. Chen, T. Ma, T. Huang, A. Yu, *ACS Appl. Mater. Interfaces*, 11 (2019) 20788–20795.